



ORIGINAL RESEARCH ARTICLE

Influential Behavior Study of Fluxes during Activated Flux Tungsten Inert Gas Welding of IRSM 41 Steel

Petla Sivateja  and Ravi Shanker Vidyarthi

Submitted: 20 September 2023 / Revised: 8 December 2023 / Accepted: 29 December 2023

Activated Flux Tungsten Inert Gas welding (A-TIG) usage is gaining popularity in the fabrication industry because of its capacity to increase the depth of penetration in a single weld pass. Increased penetration eliminates the need for joint preparation and filler material, resulting in higher productivity and lower operational costs. In the present study, IRSM 41 steel plates having 8 mm thickness were welded using tungsten inert gas welding (TIG) with and without fluxes. Six multicomponent fluxes were formulated with different oxides for the current work. The influence of the fluxes on weldment properties, such as weld bead geometry, hardness, and microstructure has been studied and presented here. The implementation of fluxes decreased bead width and increased the depth of penetration and depth/width ratio of the weldments. A thorough penetration of 8 mm was achieved in a single weld pass in Flux 6 weldments. The depth of penetration and depth/width ratio has been increased to 226% and 400%, respectively, in A-TIG weldments compared with conventional TIG weldments. The average hardness of FZ, HAZ and base metal for TIG weldment was 221 ± 24 Hv, 200.8 ± 8 Hv and 176.7 ± 5 Hv, respectively. The average hardness of FZ, HAZ, and base metal for A-TIG weldment was 255 ± 1 Hv, 221.3 ± 12 Hv, and 177 ± 5 Hv, respectively. The results (bead geometry, microstructure, and hardness) have been correlated with the input parameters.

Keywords A-TIG welding, IRSM 41 steel, marangoni convection, melting point of activating fluxes, microstructures, weld bead geometry

1. Introduction

IRSM 41 is a low alloy steel widely used in steel bridges, coastal power stations, seaports, and tanks because of its relatively better corrosion resistance and durability compared to mild steel (Ref 1). Alloying elements such as Cr, Cu, Ni and P contribute to improved corrosion resistance, tensile strength and hardness (Ref 2). In addition to this, IRSM 41 steel also exhibits excellent durability, high-temperature resistance and long service life (Ref 3). Fabrication of IRSM 41 steel requires specific welding procedures and considerations to ensure the weld joint maintains desirable strength and corrosion properties.

Conventional arc welding processes such as Shielded Metal Arc Welding (SMAW), Gas Metal Arc Welding (GMAW), Submerged Arc Welding (SAW), and Tungsten Inert Gas welding (TIG) are widely used in the fabrication of IRSM 41 steel plates (Ref 4). TIG welding is preferred over other methods because of its good surface appearance, sound quality welds, and low operational costs (Ref 5). However, a lower depth of penetration in a single pass is one of the major

disadvantages during the autogenous TIG welding process. It is suggested by the researchers that the maximum single pass depth of penetration is limited to 2-3 mm in the TIG welding process, irrespective of the welding current and travel speed (Ref 6, 7). In general, groove preparation with multiple weld passes is used for joining thick sections using TIG welding (Ref 8). This leads to additional fabrication time and cost and, thus, lower productivity. Sometimes multipass welding also induces welding defects such as angular distortion, residual stress and heterogeneous microstructure in the fusion zone. To overcome the above issues, a novel method called Activated Flux Tungsten Inert Gas welding (A-TIG) is now recommended by various researchers. In this method, activating fluxes are utilized to increase the weld penetration and lessen the number of weld passes. The Evgeny Oscarovich Paton Institute reported A-TIG welding for the first time in 1960 for joining titanium and its alloys. In this process, activating fluxes are applied on the material's surface before conventional TIG welding. The fluxes were initially used to reduce the porosity. However, while using the fluxes, researchers observed that the depth of penetration was also influenced along with porosity (Ref 9, 10).

Tseng et al. (Ref 11) used fluxes such as TiO_2 , SiO_2 , MnO_2 , and MoO_3 during the A-TIG welding of 316L stainless steels (SS). The weldments produced with SiO_2 exhibited a higher depth of penetration and reduced weld bead width compared to the other weldments. The researcher also noticed that usage of Al_2O_3 flux has a deteriorated effect on the depth of the penetration and weld bead width compared to TIG weldments. Sahu et al. (Ref 12) reported that the arc voltage was increased with the application of fluxes during the A-TIG welding of 316 SS. Due to the increase in voltage, the heat input increases in the A-TIG weldments. Vidyarthi et al. (Ref 13) observed similar results during the A-TIG welding of P91 steels. The

Petla Sivateja and Ravi Shanker Vidyarthi, Department of Mechanical Engineering, BITS-Pilani, Hyderabad Campus, Hyderabad, Telangana 500078, India. Contact e-mail: p20190045@hyderabad.bits-pilani.ac.in.

researcher reported that higher heat input, along with reverse Marangoni convection and arc constriction, contributes to a higher depth of penetration in Flux 2 weldments compared to Flux 1 and TIG weldments. Shyu et al. (Ref 14) observed that 304 SS weldments produced with SiO₂, TiO₂, Cr₂O₃ and CaO have higher retained delta ferrite than TIG weldments. The researcher reported that with the increase in retained delta ferrite, hot cracking susceptibility decreases. Due to this, A-TIG weldments exhibit lower hot cracking susceptibility than TIG weldments. The researcher observed that weldments produced with Cr₂O₃ possess lower hot cracking susceptibility than other weldments. Huang et al. (Ref 15) observed that the usage of flux composition consisting of ZnO or a mixture of ZnO + MnO₂ contributes to a reduced angular distortion in 304 SS A-TIG weldments compared to TIG weldments. The weldments produced with 20% ZnO + 80% MnO₂ possess lower angular distortion than other weldments. Fande et al. (Ref 5) observed that the chrome-manganese SS weldments produced with TiO₂ exhibit higher tensile strength than other A-TIG (SiO₂, MoO₃, CaO) and TIG weldments. The researcher reported that the increased delta ferrite in weldments with TiO₂ results in increased tensile strength than other weldments. Ramkumar et al. (Ref 16) observed that super-duplex stainless steel weldments produced with NiO flux exhibit higher impact strength than those produced with MoO₃ and SiO₂. The researcher reported that a lower amount of oxygen in the weldments produced with NiO attributed to the increased impact strength.

A-TIG welding gained popularity in the fabrication industry because it enhances weld penetration in a single pass. However, it is also clear from the literature that the effectiveness of the A-TIG welding depends on the flux composition. The weldability of the IRSM 41 has not been explored significantly with the A-TIG welding. A-TIG process could drastically reduce the fabrication cost of this material in the structure. Hence, in the current work, A-TIG welding was conducted on 8 mm thick IRSM 41 steel plates and compared with the TIG weldments. The influence of activating fluxes on weld cross section and mechanical properties is investigated. Further, a correlation is developed between the A-TIG process variables and the IRSM 41 weldments properties.

2. Materials and Methods

2.1 Base Metal

In the current work, the IRSM 41 plate, having a thickness of 8 mm, was used as a base metal. The chemical composition of IRSM 41 steel plates shown in Table 1 was analyzed with an optical emission spectrometer. The mechanical properties such as average hardness, % elongation, yield strength, and ultimate tensile strength of the IRSM 41 steel in as received condition

were 159 ± 7 Hv, 29%, 415 ± 5 MPa and 522 ± 2 MPa, respectively. An optical inverted microscope was used to investigate the microstructures acquired at the base metal. IRSM 41 principally contains a homogenous mixture of equiaxed perlite and ferrite microstructural phases, as shown in Fig. 1.

The ferritic proportion was substantially more than the perlite proportion. The line intersection method was executed in MATLAB to calculate the average grain size of the base metal. The average grain size measured was 11.7 ± 6 μm, and the distribution of the grain size is presented in Fig. 1.

The phases generated while cooling IRSM 41 steel at different cooling rates are depicted in Fig. 2. The annotations shown in Fig. 2 are B – Bainite, M - Martensite, F- Ferrite, and P - Pearlite, and the subscripts “s” and “f” imply “reaction start” and “ reaction finish,” respectively.

2.2 Welding Procedure

IRSM 41 plates with 160 mm (length) × 110 mm (width) × 8 mm (thickness) were extracted using wire EDM. Prior to the welding, the extracted plate had undergone grinding, polishing, and thorough cleaning with acetone. Subsequently, bead-on plate welding was done along 160 mm length at the center of the prepared plates using Tungsten inert gas welding with and without fluxes. Six multicomponent fluxes have been prepared with SiO₂, TiO₂, Cr₂O₃, CuO, MoO₃, ZnO and NiO and used during the A-TIG welding. The varying weight percentages in different flux compositions are provided in Table 2. Prior to welding, the fluxes were coated over the surface of the plates with a paintbrush (shown in Fig. 3). Flux coating density (flux coating quantity per unit surface area) maintained was around 4-6 mg/cm². A direct current straight polarity (DCSP) power source was employed to perform welding. Arc length, welding speed and welding current during all the welding experiments used in the current work were 220A, 80 mm/min and 3 mm, respectively. A 2% thoriated electrode with a 3.2 mm diameter and 60° electrode tip angle was used during the welding. A 99% pure argon gas was provided at a 10 liters/minute flow rate to protect the weld area from atmospheric contamination.

2.3 Characterization Techniques

Samples were extracted from the weldments produced with and without fluxes and underwent polishing. Later, the metallographic examination was conducted on the polished samples. A stereo microscope (Model: M, make: Metzger) was used to investigate the cross section of the IRSM 41 weldments. Using an inverted optical microscope (Model: IM7200, make: Meiji Techno), the microstructures at various regions (base metal, HAZ and FZ) were acquired and analyzed. Field emission scanning electron microscope analysis (FE-SEM) (Model: Apreo LoVac, make: FEI) was carried out to find the

Table 1 IRSM 41 base metal chemical composition

Elements	Nb	Al	Mn	C	Ni	Cr	S	Si	Ti	P	Fe
Wt.%	0.004	0.018	0.38	0.08	0.22	0.53	0.009	0.29	0.003	0.087	Balanced

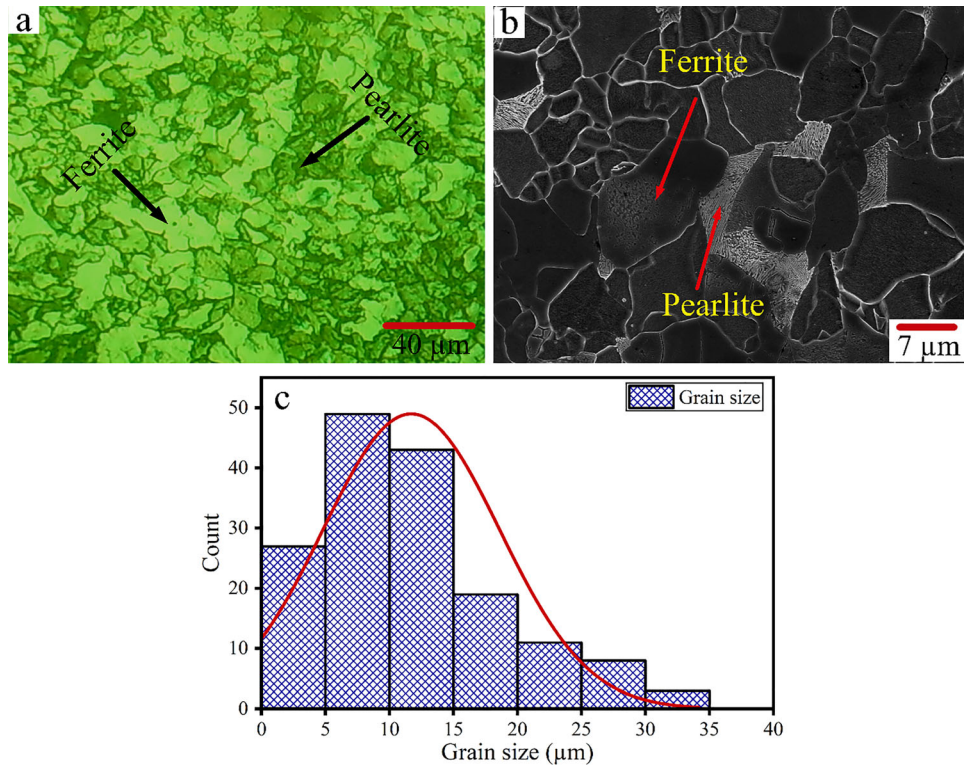


Fig. 1 Schematics shows the base metal (a) optical microstructure, (b) FESEM image and (c) distribution of grain size

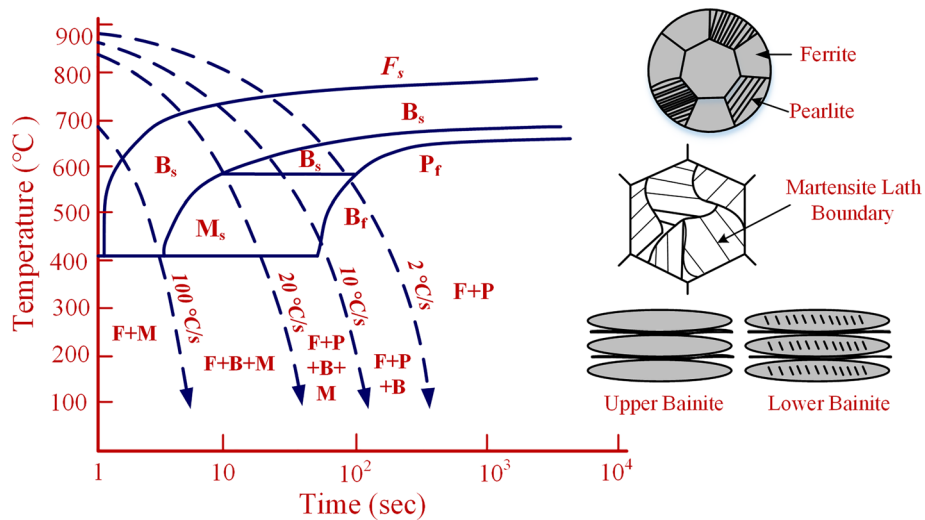


Fig. 2 Schematic depiction of the phases produced while cooling IRSM 41 steel at different cooling rates

presence of precipitates. The weldment's FZ composition was evaluated with energy-dispersive x-ray spectroscopy (EDS) (Model: Apreo LoVac, Make: FEI). X-ray diffraction analysis (XRD) (Model: XTALAB, make: Rigaku Oxford) was done at a scan rate of 0.02 seconds per step to find the position of the phases present in the FZ of the weldments. The mechanical characterization of the IRSM 41 weldments was evaluated in terms of Vickers hardness. Vickers hardness testing was conducted at 0.2 kgf load, with the readings taken at 0.5 mm intervals in the hardness tester (Make: Mitutoyo, Model: HM-200). During the hardness testing, a dwell time of 10 seconds

was maintained. ASTM E384 standards were followed during Vickers hardness testing.

3. Results and Discussion

3.1 Visual Inspection and Macroscopic Analysis

The weldments had undergone visual inspection just after welding to find traces of surface imperfections such as cavities and surface cracks. The front and back sides of the welded plates are shown in Fig. 3. After the visual inspection, the

Table 2 Composition of fluxes used

Flux used	Wt.% of various fluxes used						
	SiO ₂	TiO ₂	Cr ₂ O ₃	CuO	MoO ₃	ZnO	NiO
Flux 1	6-7	25-26	6-7	6-7	6-7	25-26	25-26
Flux 2	7-8	30-31	7-8	7-8	7-8	7-8	30-31
Flux 3	18-19	18-19	18-19	18-19	4-5	4-5	18-19
Flux 4	4-5	16-17	16-17	16-17	16-17	16-17	16-17
Flux 5	30-31	30-31	7-8	7-8	7-8	7-8	7-8
Flux 6	25-26	6-7	6-7	25-26	25-26	6-7	6-7

samples were extracted for macroscopic, microscopic and hardness analysis. The cross section of the weldments produced with and without applying fluxes is presented in Fig. 4. It is observed that the weldments produced with the application of fluxes exhibit higher penetration compared to the weldments produced without flux. The depth of penetration for TIG, Flux 1, Flux 2, Flux 3, Flux 4, Flux 5, and Flux 6 weldments were 2.45 ± 0.5 mm, 3.62 ± 0.4 mm, 4.53 ± 0.5 mm, 5.67 ± 0.4 mm, 6.49 ± 0.5 mm, 7.12 ± 0.5 mm and 8 mm, respectively. The weld bead width of TIG, Flux 1, Flux 2, Flux 3, Flux 4, Flux 5, and Flux 6 weldments were 13.74 ± 0.5 mm, 12.62 ± 0.5 mm, 12.5 ± 0.4 mm, 10.62 ± 0.5 mm, 10.57 ± 0.3 mm, 9.84 ± 0.5 mm and 9.37 ± 0.4 mm, respectively. The depth/width ratio of TIG, Flux 1, Flux 2, Flux 3, Flux 4, Flux 5, and Flux 6 weldments were 0.17 ± 0.04 , 0.28 ± 0.02 , 0.36 ± 0.03 , 0.53 ± 0.02 , 0.61 ± 0.03 , 0.72 ± 0.02 and 0.85 ± 0.03 , respectively. Among all the weldments, Flux 6 weldments exhibit minimum weld bead width and maximum depth of penetration, depth/width ratio. On the other hand, the maximum weld bead width and minimum depth of penetration, depth/width ratio are observed in TIG weldments. A thorough penetration in an 8 mm thick plate was achieved in the weldments produced with Flux 6. The depth of penetration is increased by 226% in Flux 6 weldments (8 mm) compared to TIG weldments (2.45 ± 0.5 mm). The weld bead width is reduced by 32% in Flux 6 weldments compared to TIG weldments. Consequently, a rise of 400% in the depth/width ratio is observed. The change in depth of penetration, weld bead width and depth/width ratio for A-TIG and TIG weldments is depicted in Fig. 5. It is observed that the weldments produced with flux possess lower weld bead width compared to the weldments fabricated without flux. In contrast, the depth of penetration and depth/width ratio are observed to be higher in A-TIG weldments than in TIG weldments.

Reverse Marangoni convection and arc constriction are considered as the major contributing mechanisms for improved penetration in A-TIG welding (Ref 17). During TIG welding, the weld pool center experiences higher temperatures, whereas the periphery of the weld pool exhibits lower temperatures. As the temperatures increase, the surface tension reduces. Hence, lower surface tension is observed at the weld pool center because of higher temperatures. Higher surface tension is observed at the periphery due to lower temperatures. Marangoni convection states that fluid always flows from low surface tension to high surface tension. Hence, the molten metal flows from the weld pool center to the periphery in TIG weldments, as presented in Fig. 6(a). This resulted in shallow penetration with wider weld bead width. The usage of fluxes during A-TIG welding alters the surface tension-temperature

gradient from negative to positive. As a result, with increases in temperature, the surface tension increases. In agreement with the above, researchers demonstrated higher surface tension at the center and lower surface tension at the periphery of the A-TIG weld pool (Ref 13). Due to the positive surface tension temperature gradient, the molten metal flows radially inwards toward the weld pool center (shown in Fig. 6(b)), resulting in deeper penetration and narrow weld bead width (Ref 18). The other most accepted mechanism is arc constriction. It is stated that the coated flux dissociates during the welding (Ref 19). The dissociated molecules form an ionic vapor cloud around the arc. The vapor cloud captures the electrons from the arc's outer periphery. Restricting the current flow toward the arc center and thus increases the current density. Higher current densities at the anode root lead to an increased heat density at the anode root, thus supporting a deeper and narrower penetration (Ref 20).

Apart from arc constriction and reversal in Marangoni convection, heat input variation at the same current may also influence the weld bead geometry. The heat input for the A-TIG and TIG weldments is determined with Eq 1.

$$Q_I = \eta VI/s \quad (\text{Eq 1})$$

where η , I , s , V and Q_I are process efficiency, welding current, welding speed, welding voltage and heat input, respectively. The value of efficiency (η) considered in the current work is 60%, as suggested by the American Welding Society (Ref 21). The welding voltage generated during the welding directly influences the heat input. Therefore, the voltage during the welding was recorded, and the average of the same is considered for calculating the heat input. It is observed that the average welding voltage was higher during A-TIG welding in comparison with TIG welding. Besides this, welding voltage was found to be different with different flux compositions. The average welding voltage observed during welding was 14.22 ± 0.5 V. Maximum welding voltage was observed with Flux 6 (15.45 ± 0.5 V), and the minimum was with TIG (13 ± 0.5 V) welding. Corresponding to welding voltage, the heat input is calculated and presented in Fig. 7(a). A maximum heat input (1.52 ± 0.5 kJ/mm) is witnessed during welding with Flux 6, and a minimum heat input (1.28 ± 0.5 kJ/mm) is noticed in TIG weldments. The activating fluxes applied during welding exhibit high electric resistivity. Due to this, they act as insulators between the tungsten electrode and plate surface and obstruct the current flow. In order to retain a stable flow of current, the arc voltage is increased. Thus, higher voltage is observed in A-TIG weldments than in TIG weldments. Higher inputs produced due to higher voltage may result in more fusion zone area in the weldments. The combination of reversal of Marangoni and high heat input could produce higher weld penetration.

The variation of depth of penetration with heat input for TIG and A-TIG weldments is presented in Fig. 7. Figure 7 elucidates that as the heat input increases from TIG to Flux 6 weldments, the depth of penetration increases. The increase in heat input due to higher voltage may be attributed to the rise of depth of penetration. Based on the above results, it is elucidated that higher heat input, better arc constriction, and reversal Marangoni convection may be attributed to the lower weld width bead and higher depth of penetration in Flux 6 weldments. Flux 6 A-TIG weldment is used along with TIG weldment for further analysis.

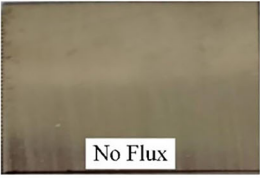
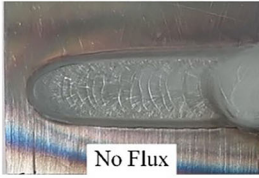
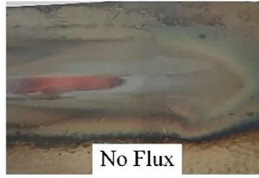
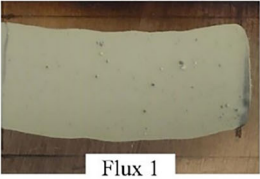
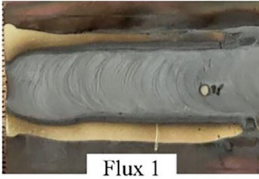
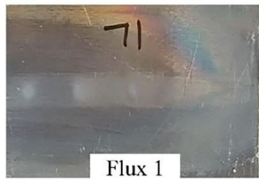
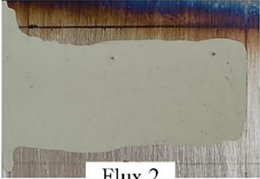
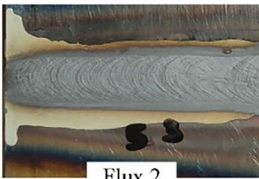

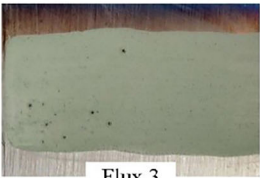
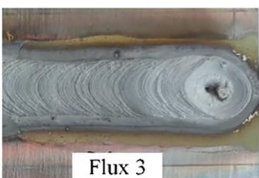

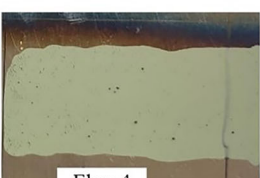
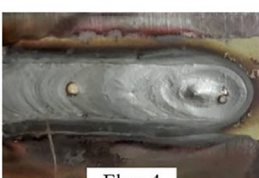


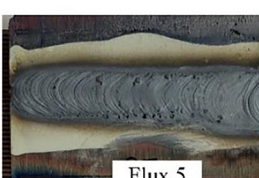
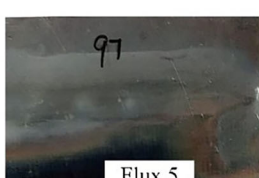
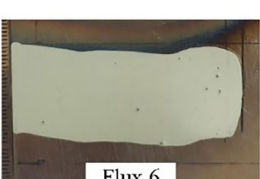
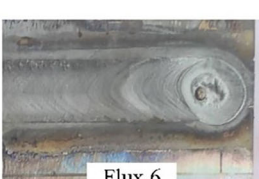

Plates before welding	Front side of the welded Plates	Back side of the welded Plates
 No Flux	 No Flux	 No Flux
 Flux 1	 Flux 1	 Flux 1
 Flux 2	 Flux 2	 Flux 2
 Flux 3	 Flux 3	 Flux 3
 Flux 4	 Flux 4	 Flux 4
 Flux 5	 Flux 5	 Flux 5
 Flux 6	 Flux 6	 Flux 6

Fig. 3 IRSM 41 plates (a) prior to welding, (b) front side after welding and (c) backside after welding

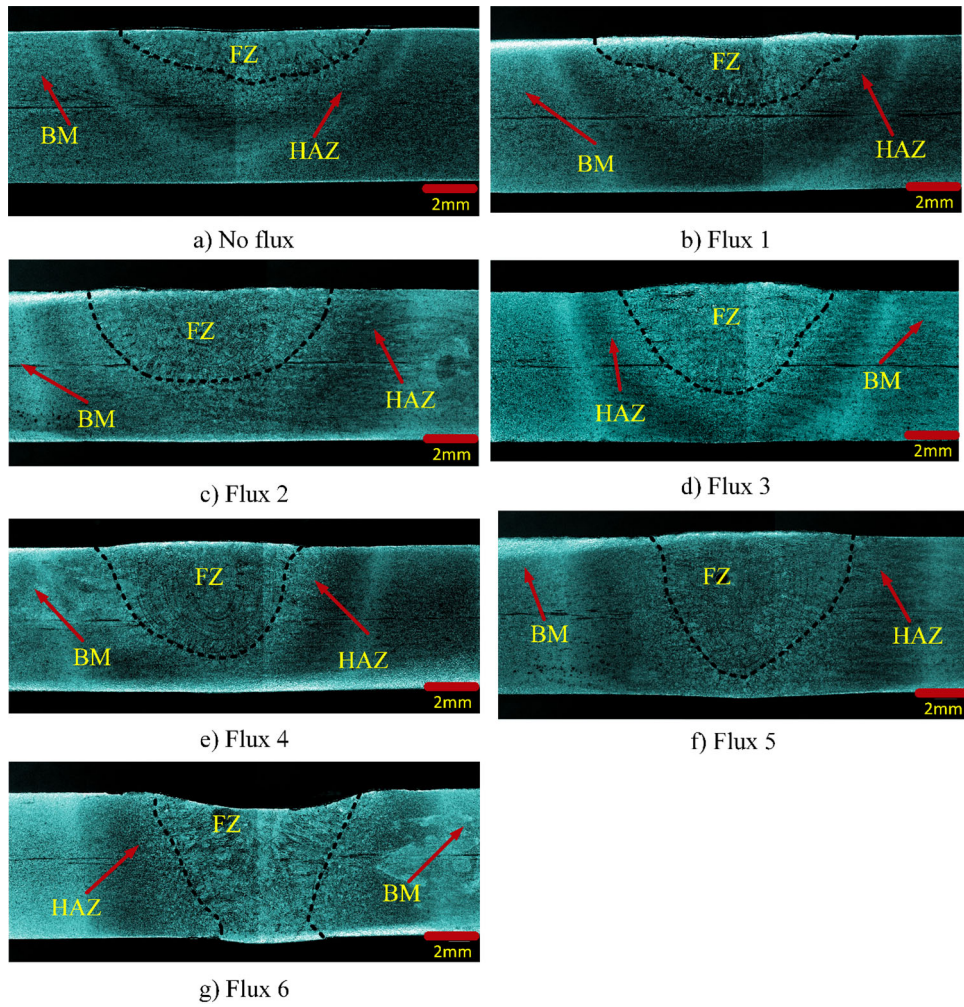


Fig. 4 Macrographs of the weldments produced (a) without and (b-g) with fluxes

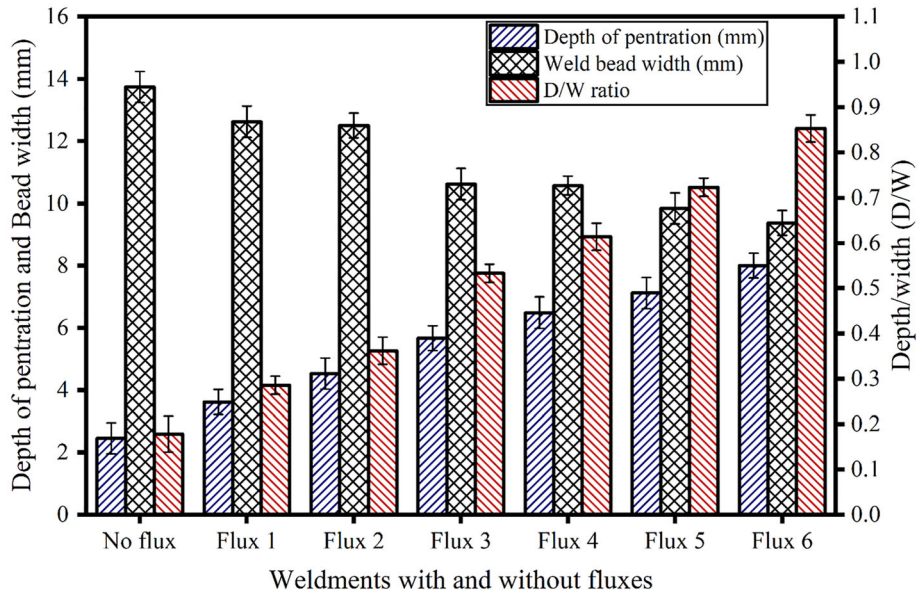


Fig. 5 Weld bead geometry (depth of penetration, weld bead width and depth/width) of the weldments

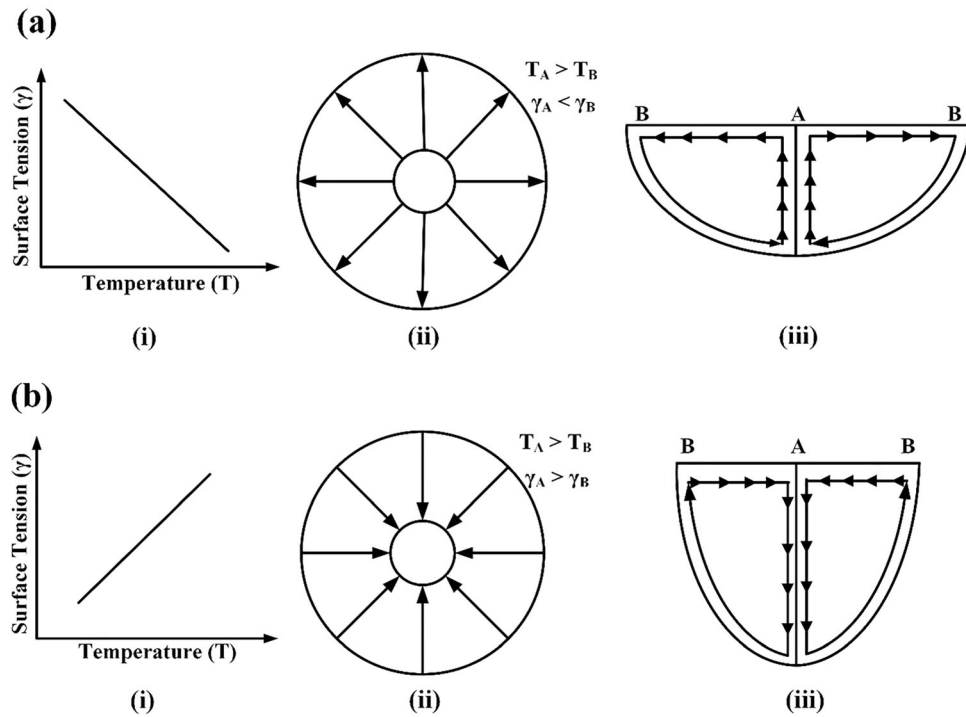


Fig. 6 Schematics represent here (i) relation between surface tension and temperature, (ii) fluid flow and (iii) expected weld bead geometry; in (a) without flux and (b) with flux condition

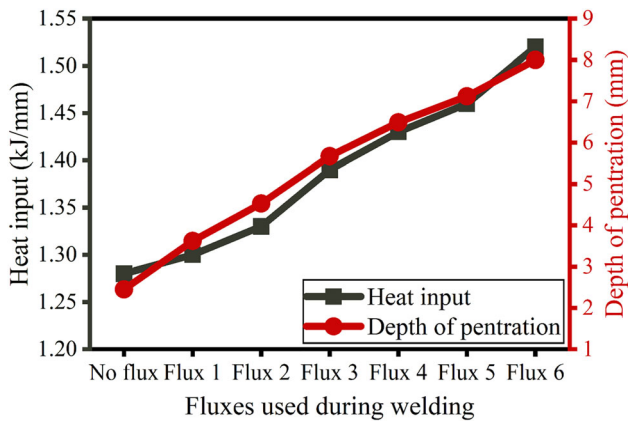


Fig. 7 Graph shows the variation of depth of penetration with the heat input for TIG and A-TIG weldments

3.2 Microstructural Analysis

The microstructures obtained at various regions (unaffected base metal, HAZ, and FZ) of TIG and A-TIG weldments are presented in Fig. 8 and Fig. 9, respectively. Microstructural phases such as martensite, grain boundary ferrite (GBF), acicular ferrite (AF) and widmanstatten ferrite (WF) were observed in the FZ of TIG (Fig. 8(a, d)) and A-TIG weldments (Fig. 9(a, d)) (Ref 22). The above-mentioned microstructural phases are produced in the FZ occur due to the interaction among various factors such as weld thermal cycle, cooling rate, prior austenite grain size and chemical composition. The heat input during A-TIG (1.52 ± 0.5 kJ/mm) weldments was relatively more than the TIG (1.28 ± 0.5 kJ/mm) weldments. This may result in higher temperatures, causing A-TIG weldments to cool more slowly than the TIG weldments. Slow

cooling rates due to higher inputs may promote the formation of widmanstatten ferrite and acicular ferrite (Ref 23). Coarser GBF was witnessed at FZ of A-TIG. In contrast, FZ of TIG possesses finer GBF (shown in Fig. 8 and Fig. 9). At lower cooling rates, the solidification time increases, increasing the retained austenite time and causing grain coarsening (Ref 24). Hence, A-TIG weldments with higher heat input than the TIG weldments exhibit coarsened GBF because of lower cooling rates. Adak et al. (Ref 25) also illustrated the formation of finer GBF at lower heat inputs and coarser GBF at higher heat inputs. Further, faster cooling during welding may contribute to the formation of martensite in the FZ of TIG and A-TIG weldments (Ref 26). Minor variations in the microstructural phases could be attributed to slightly higher heat input due to close circuit voltage variation during A-TIG and TIG welding process.

The presence of widmanstatten ferrite, acicular ferrite, grain boundary ferrite (GBF) and martensite was observed in the HAZ of both weldments, and the same is presented in Fig. 8(b, e) and Fig. 9(b, e). Adak et al. (Ref 25) reported that the temperature in HAZ was around 910 °C. At these lower temperatures, a significant ferritic-austenitic transformation does not occur. Due to this, smaller proportions of martensite were produced in HAZ during the cooling of austenite. The lower heat inputs resulting from lower temperatures in HAZ also regulate the formation of acicular ferrite and widmanstatten ferrite generation. Thus, lower proportions of martensite, acicular ferrite and widmanstatten ferrite were witnessed in HAZ. Microstructural phases such as ferrite and perlite were observed in the unaffected base metal of both weldments (shown in Fig. 8(c, f) and Fig. 9(c, f)) (Ref 27). FE-SEM analysis was carried out on TIG and A-TIG weldments by acquiring micrographs at FZ, HAZ and base metal, as presented in Fig. 8(g-i) and Fig. 9(g-i). The FZ and HAZ of both

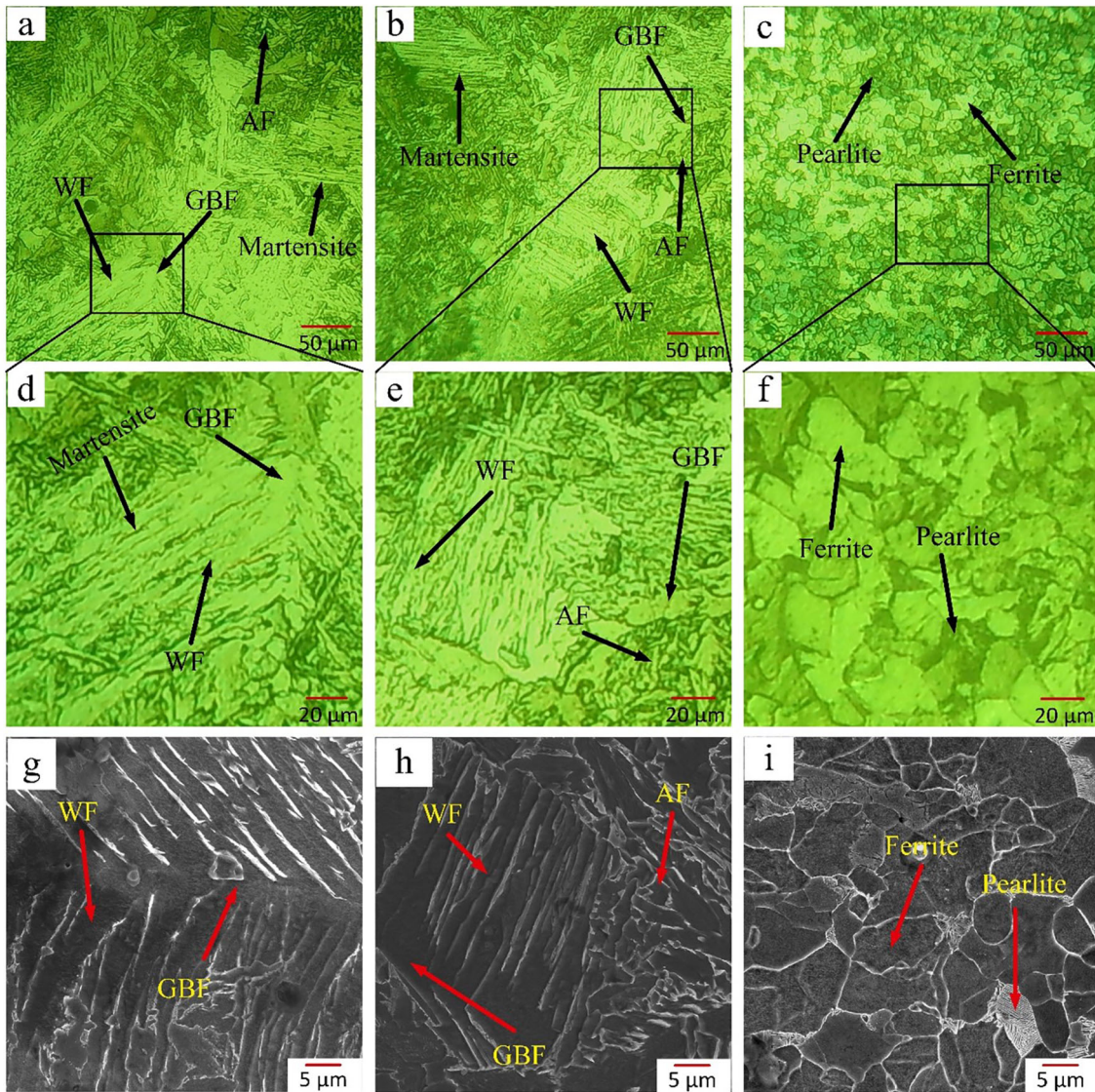


Fig. 8 Microstructures of TIG welded sample in (a, d & g) FZ, (b, e & h) HAZ and (c, f & i) unaffected base metal

weldments consist of grain boundary ferrite, widmanstatten ferrite, martensite and acicular ferrite, whereas in the unaffected base metal, the presence of ferrite and pearlite was observed.

The microstructural phase distribution in the FZ of TIG and A-TIG weldments is estimated through the Schaeffler diagram by using chromium and nickel equivalents. FZ chemical composition of the TIG and A-TIG weldments is presented in Table 3.

The chromium equivalent (Cr_{eq}) and nickel equivalent (Ni_{eq}) are calculated using Eq 2 and Eq 3 (Ref 28).

$$Cr_{eq} = \%Cr + \%Mo + 1.5\%Si + 0.5\%Nb \quad (\text{Eq 2})$$

$$Ni_{eq} = \%Ni + 30\%C + 0.5\%Mn \quad (\text{Eq 3})$$

The Cr_{eq} and Ni_{eq} equivalents for TIG weldments are 1.043 and 2.79, respectively. The Cr_{eq} and Ni_{eq} equivalents for A-TIG weldments are 1.133 and 3.01, respectively. The Cr_{eq} and Ni_{eq} equivalents values of TIG and A-TIG weldment suggest the presence of ferritic–martensitic (F + M) combination in the FZ, as shown in Fig. 10. The predicted microstructural phases using

the Schaeffler diagram are found to be in good agreement with optical and FE-SEM microstructures.

XRD analysis was performed on TIG and A-TIG weldments to detect phases present at the FZ, and the recorded spectra is shown in Fig. 11. Figure 11 reveals that the α -Iron phase (BCC, Ferrite) and martensite were the principal constituent witnessed in TIG and A-TIG weldments (Ref 29, 30). In addition to this, low-intensity cementite peaks were also observed in both weldments. Other phases, such as austenite, were not detected in the XRD patterns, it may be due to lower volume fractions. The detected peak intensities in XRD analysis are used to determine the volume fraction of the various phases present in A-TIG and TIG weldments by using the normalized intensity ratio (NIR) method (Ref 31). The NIR of the x phase is determined from Eq 4 (Ref 28). In the NIR method, major peaks are considered for calculating the volume fraction. The calculated NIR values of various phases in TIG and A-TIG are presented in Table 4. The fraction of ferrite (63.08%) and martensite (33.81%) obtained by the NIR method in A-TIG

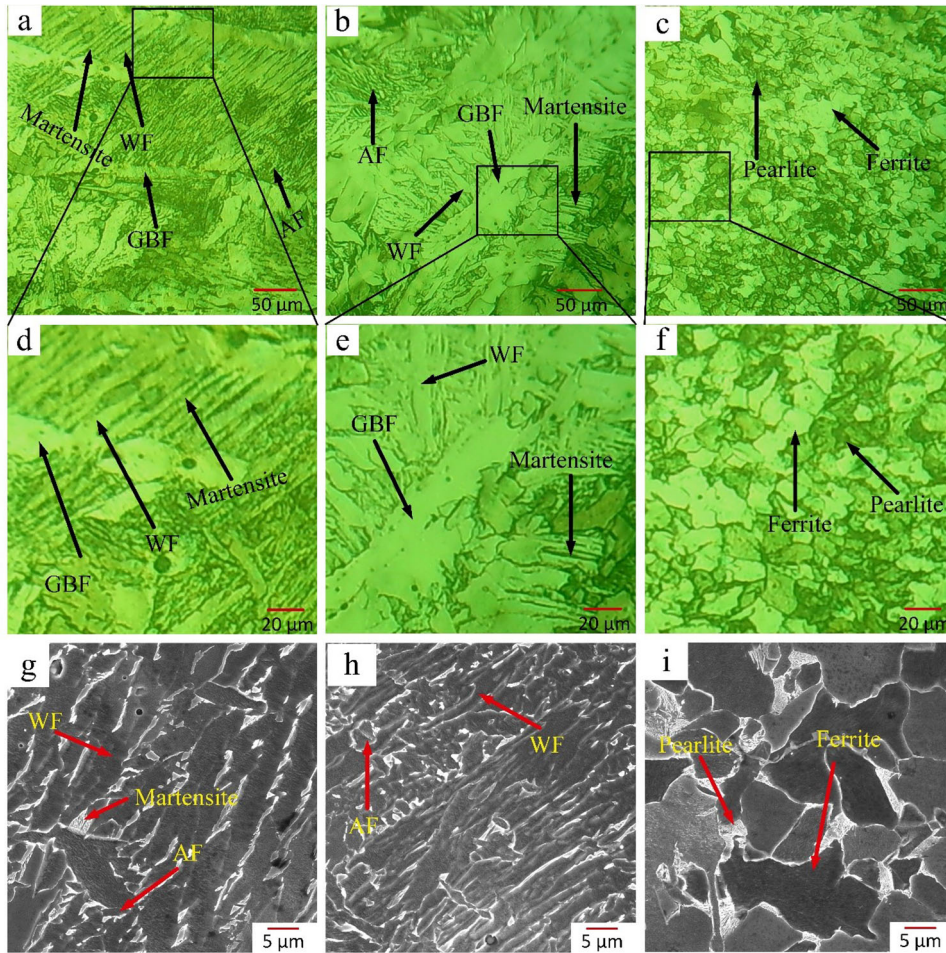


Fig. 9 Microstructures of A-TIG weld sample in (a, d & g) FZ, (b, e & h) HAZ and (c, f & i) unaffected base metal

Table 3 Alloying elements with predicted microstructure in the A-TIG and TIG weld fusion zone

Elements wt.%	C	Mn	Nb	Si	Cr	Ni	Mo	Cr _{eq}	Ni _{eq}	Predicted microstructure
TIG	0.028	0.373	0.002	0.504	0.415	0.265	0.054	1.22	1.29	F + M
A-TIG	0.038	0.365	0.004	0.300	0.525	0.218	0.004	0.979	1.54	F + M

weldments is in good agreement with the predicted ferrite and martensite through the Schaeffler diagram.

$$NIR_x = \frac{I_x - I_{back}}{\sum_{x=1}^n I_x - nI_{back}} \quad (\text{Eq 4})$$

During the FESEM analysis, a very small number of precipitates were observed in the FZ of A-TIG and TIG weldments. EDS analysis suggested that the precipitates were mainly oxides of aluminum and ferrous, as shown in Fig. 12 and Fig. 13. The sizes of the aluminum and ferrous oxides were found $2.5 \pm 0.1 \mu\text{m}$ and $6 \pm 0.1 \mu\text{m}$, respectively. Aluminum is generally used during the manufacturing of IRSM 41 steel to remove excess oxygen (Ref 32). Therefore, it is expected that traces of aluminum oxide observed during FESEM analysis are because of the base metal composition (Table 1). Besides this, inclusions enriched with Si, Ti, O, and Cr were also observed (Fig. 14). The size of the inclusions found in A-TIG weldments

was $4 \pm 0.3 \mu\text{m}$. The presence of the inclusions in A-TIG weldments may be attributed to the flux used during the A-TIG welding. Similar inclusions were also reported by Wan et al. (Ref 33). It is stated that the inclusions consisting of (Mn, Si, O, Ti, and Al) promote the acicular ferrite generation, resulting in improved hardness and strength of weldments. Hence, the inclusions observed in A-TIG weldments of the current work may contribute to improved hardness compared to TIG weldments. On the other hand, the precipitates observed in both weldments were very low in proportions and thus does not have a significant influence on the mechanical properties (Ref 34).

3.3 Hardness Analysis

The hardness of A-TIG and TIG weldments was measured in XX and YY directions, and the same is shown in Fig. 15(a). The distribution of hardness across base metal, HAZ and FZ for

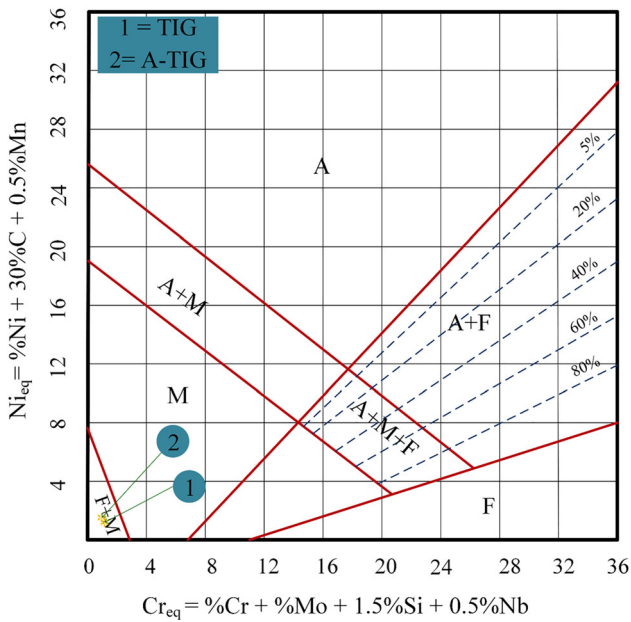


Fig. 10 Schaeffler diagram representing fusion zone of A-TIG and TIG weldments having different Cr-Ni equivalent coordinates

both weldments is presented in Fig. 15(b). In both TIG and A-TIG weldments, the hardness profile increases from the weld center to the fusion line; afterward, it decreases toward the base metal. The average hardness of FZ, HAZ and base metal for TIG weldment were 221 ± 24 Hv, 200.8 ± 8 Hv and 176.7 ± 5 Hv, respectively. The average hardness measured across FZ, HAZ, and base metal for A-TIG weldment were 255 ± 1 Hv, 221.3 ± 12 Hv, and 177 ± 5 Hv, respectively. In both TIG and A-TIG weldments, FZ exhibits higher average hardness than HAZ and base metal. The increased hardness of the FZ could be attributed to the existence of martensite and acicular ferrite (Ref 26). The presence of cementite in the FZ of TIG and A-TIG weldments, as witnessed during the XRD analysis, may also increase the FZ hardness. Relatively higher hardness of A-TIG FZ compared to TIG FZ could be due to the proportional change of martensite as observed during the microstructural study. HAZ of both weldments exhibits higher hardness compared with the base metal. The presence of martensite and acicular ferrite in smaller proportions contributes to the enhanced hardness in HAZ (Ref 35). In addition to this, the weldments produced with A-TIG exhibit higher hardness than the TIG weldments.

The hardness distribution from the top face to the root face is presented in Fig. 15(c). In TIG weldments, the hardness was decreased from the top face to the root face. Since FZ exists to a certain distance from the top face, followed by HAZ and base

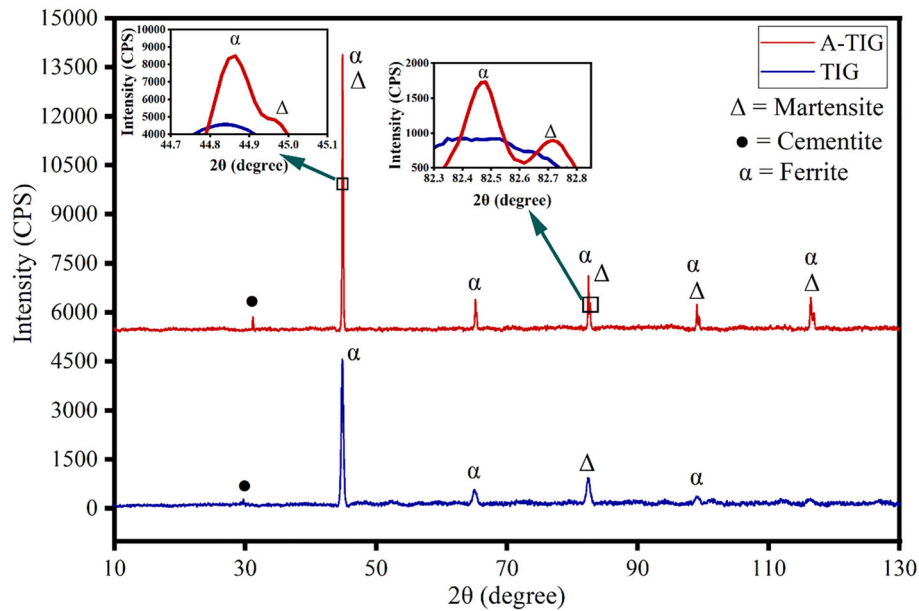


Fig. 11 X-ray diffraction patterns of the A-TIG and TIG fusion zone

Table 4 Relative phase intensities of different phases detected in the fusion zone of A-TIG and TIG weldments

Weldment	Phase detected	I ₁	I ₂	I ₃	I _{back}	NIR%
TIG	Ferrite	4500.98	2	79.37
	Martensite	...	917.27	...	2	16.17
	Cementite	264.03	...	4.65
A-TIG	Ferrite	8496.62	2	63.08
	Martensite	...	4554.87	...	2	33.81
	Cementite	428.91	2	3.18

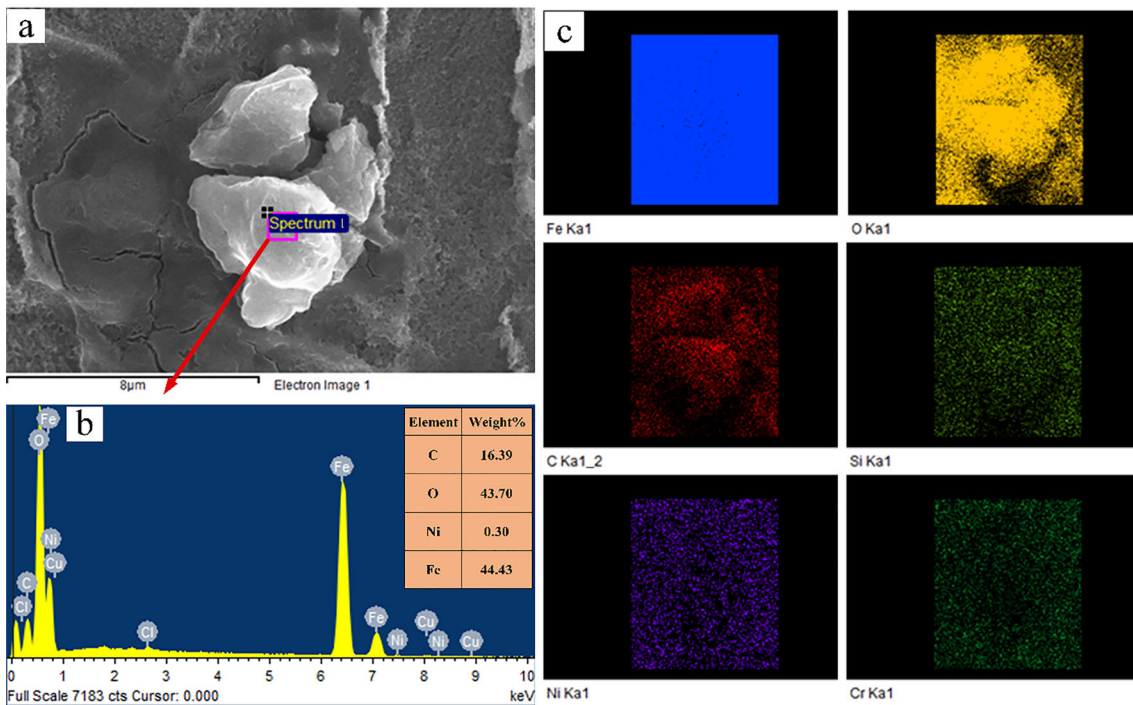


Fig. 12 EDS analysis and area mapping of the ferrous oxide precipitates observed in TIG and A-TIG weld fusion zone

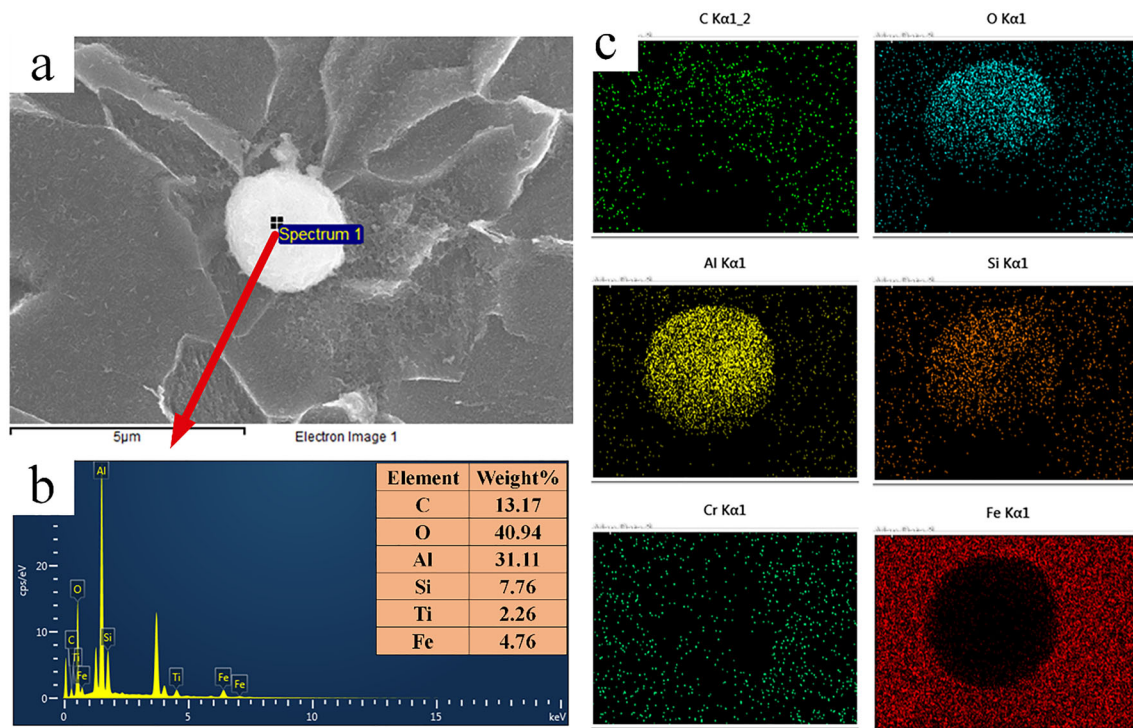


Fig. 13 EDS analysis and area mapping of the aluminum oxide precipitates observed in A-TIG and TIG weld fusion zone

metal, a considerable proportion of martensite and acicular ferrite in FZ leads to a superior hardness than in the HAZ and base metal. Hence, a decremental hardness profile is witnessed from the top to the root face. Whereas, in A-TIG weldments, a substantial difference in hardness distribution is not noticed

from the top face to the root face. Due to a thorough penetration, the entire region from the top to the root face is occupied with FZ. Existence of similar microstructural phases with minor deviations in their proportion may be attributed to the marginal variation in the hardness distribution.

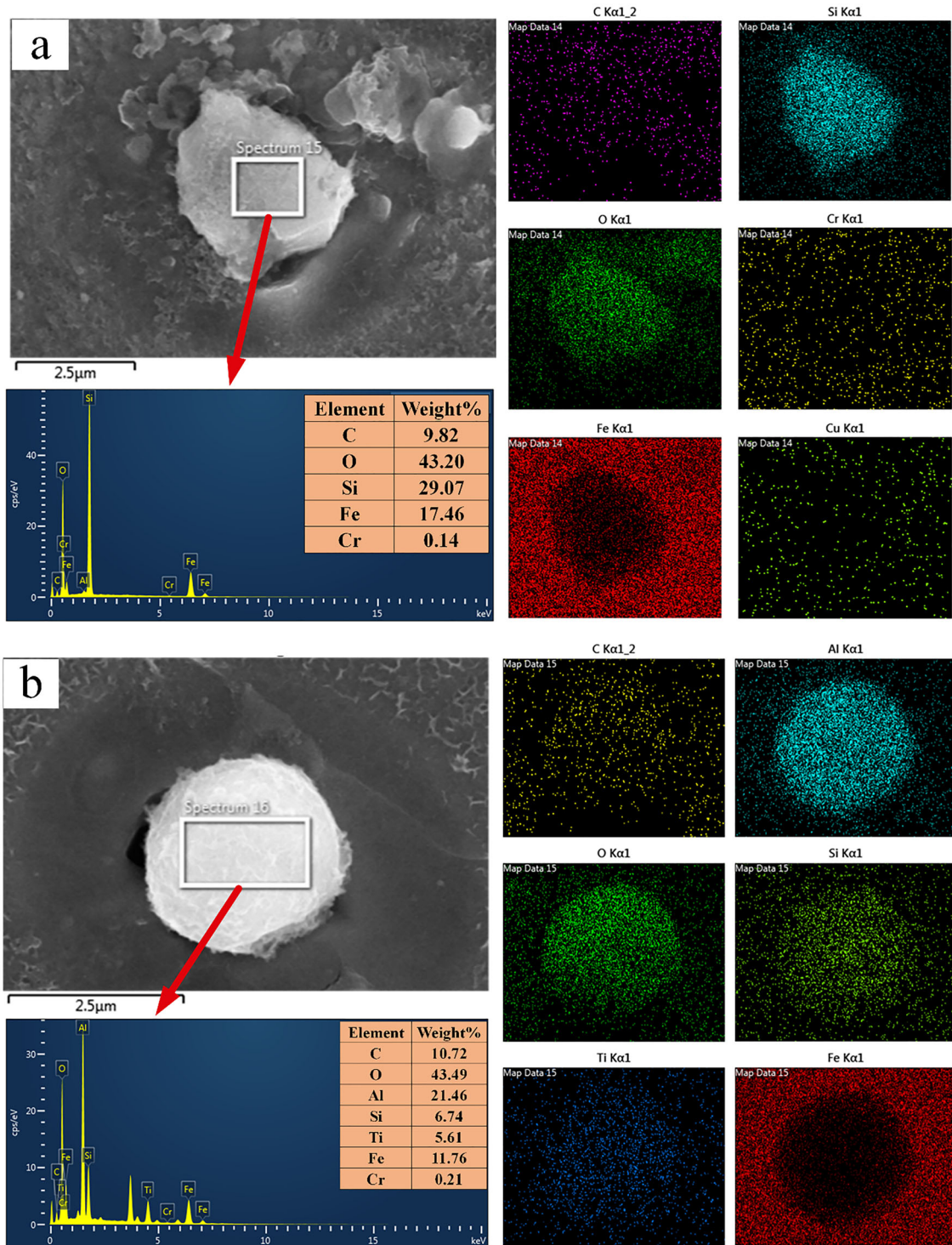


Fig. 14 (a & b) EDS analysis and area mapping of the inclusions observed in the fusion zone of the weldments

4. Conclusions

In the current work, TIG welding was conducted on IRSM 41 plates with and without the application of fluxes. Based on the macrostructural, microstructural and hardness study, the following conclusions are drawn:

- A reduced weld bead width and an enhanced depth of penetration, depth/width ratio were noticed in weldments

produced with fluxes. The depth of penetration increased to 226% in A-TIG weldments compared to TIG weldments at the same welding process parameters.

- A full penetration of 8 mm was achieved in a single pass by applying Flux 6 during the A-TIG welding of IRSM 41 plates.
- Arc constriction and reverse Marangoni convection are the principal mechanisms contributing to a lower weld bead width and higher depth of penetration in the A-TIG weldments compared to the TIG weldments.

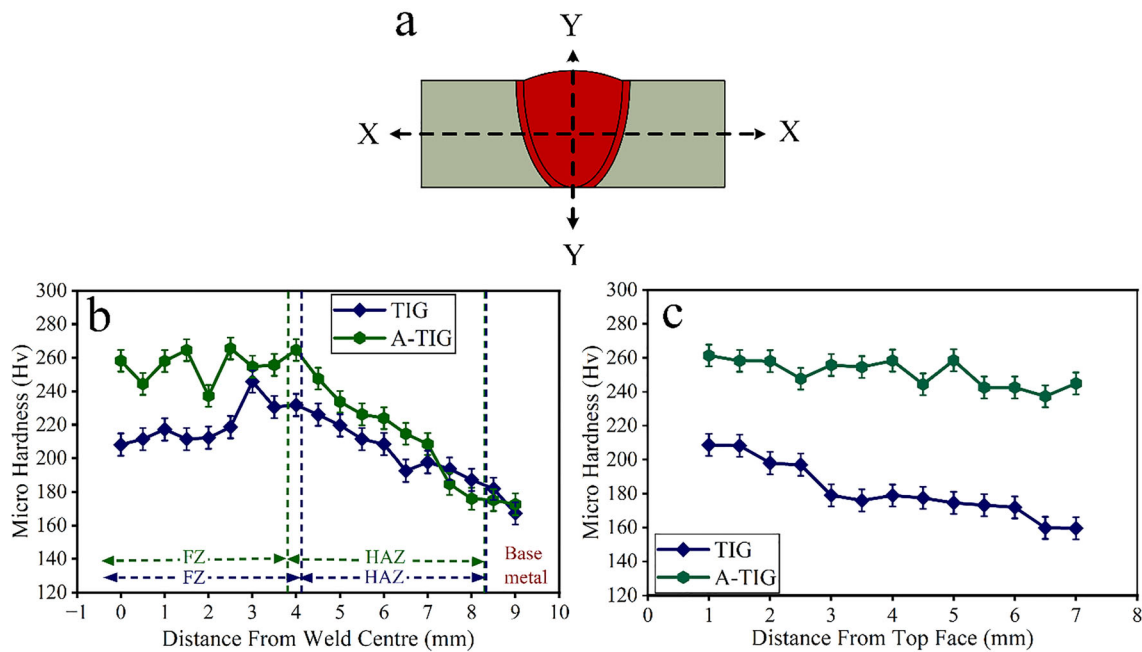


Fig. 15 Schematics illustrate (a) pattern of hardness measurement, (b) hardness distribution across X-X direction and (c) hardness distribution across Y-Y direction of the A-TIG and TIG weldments

- Microstructural study reveals the presence of martensite, widmanstatten ferrite, acicular ferrite and grain boundary ferrite in the FZ of TIG and A-TIG weldments. HAZ of all the weldments contains ferrite, perlite, martensite, GBF, AF, WF.
- Microhardness analysis elucidates that the average hardness of the FZ of both TIG and A-TIG weldments was higher compared to HAZ and base metal. The increased FZ hardness was because of the existence of acicular ferrite, martensite and a smaller proportion of cementite.

Author Contributions

All authors contributed to the study conception and design. Material preparation, data collection and analysis were performed by PS and RSV. The first draft of the manuscript was written by PS, and all authors commented on previous versions of the manuscript. All authors read and approved the final manuscript.

Funding

The authors declare that they did not receive any funding, grants, or other support during the preparation of this manuscript.

Competing interests

The authors declare that they have no known competing financial interests or personal relationships that could have appeared to influence the work reported in this paper.

References

1. C. Dong, A. Zhao, X. Wang, Q. Pang, and H. Wu, Microstructure and Properties of 1100 MPa Grade Low-Carbon Hot-Rolled Steel by Laser Welding, *J. Iron. Steel Res. Int.*, 2018, **25**(2), p 228–234. <https://doi.org/10.1007/s42243-018-0025-3>
2. J.R. Deepak, V.B. Raja, K.R. Kavitha, K.G. Reddy, and M. Venkat, Microstructure and Metallurgical Property Investigation of Welded IRSM 41-97 Rail Steel Joints, *Mater. Today Proc.*, 2021, **1**(47), p 4827–4832. <https://doi.org/10.1016/j.matpr.2021.06.056>
3. D. Zhao, Y. Bezgans, N. Vdonin, and V. Kvashnin, Mechanical Performance and Microstructural Characteristic of Gas Metal Arc Welded A606 Weathering Steel Joints, *Int. J. Adv. Manuf. Technol.*, 2022, **119**(3–4), p 1921–1932. <https://doi.org/10.1007/s00170-021-08383-7>
4. P. Beeharry and B.Y. Surnam, Atmospheric Corrosion of Welded Mild Steel, *Mater. Today Proc.*, 2018, **5**(2), p 7476–7485. <https://doi.org/10.1016/j.matpr.2017.11.419>
5. A.W. Fande, R.V. Taiwade, and P.C. Sekhar, Microstructure, Mechanical, and Electrochemical Evaluation of Chrome-Manganese Stainless Steel Activated Tungsten Inert Gas Welded Joint, *J. Mater. Eng. Perform.*, 2022, **31**(11), p 9431–9447
6. M. Vasudevan, Effect of A-TIG Welding Process on the Weld Attributes of Type 304LN and 316LN Stainless Steels, *J. Mater. Eng. Perform.*, 2017, **26**(3), p 1325–1336
7. A. Toppo, M.G. Pujar, B. Arivazhagan, M. Vasudevan, C. Mallika, and M.U. Kamachi, Corrosion Behaviour of 304LN Activated Tungsten Inert Gas and Flux-Cored Arc Weld Metals, *Corros. Eng. Sci. Technol.*, 2016, **51**(4), p 295–307
8. P. Sharma and D.K. Dwivedi, Comparative Study of Activated Flux-GTAW and Multipass-GTAW Dissimilar P92 Steel-304H ASS Joints, *Mater. Manuf. Process.*, 2019, **34**(11), p 1195–1204. <https://doi.org/10.1080/10426914.2019.1605175>
9. H. Rana, V. Badheka, P. Patel, V. Patel, W. Li, and J. Andersson, Augmentation of Weld Penetration by Flux Assisted TIG Welding and Its Distinct Variants for Oxygen Free Copper, *J. Mater. Res. Technol.*, 2021, **10**, p 138–151. <https://doi.org/10.1016/j.jmrt.2020.12.009>
10. A. Kulkarni, D.K. Dwivedi, and M. Vasudevan, Dissimilar Metal Welding of P91 Steel-AISI 316L SS with Incoloy 800 and Inconel 600 Interlayers by Using Activated TIG Welding Process and Its Effect on

- the Microstructure and Mechanical Properties, *J. Mater. Process. Technol.*, 2019, **274**, p 1–14. <https://doi.org/10.1016/j.jmatprotec.2019.116280>
11. K.H. Tseng and C.Y. Hsu, Performance of Activated TIG Process in Austenitic Stainless Steel Welds, *J. Mater. Process. Technol.*, 2011, **211**(3), p 503–512
 12. N. Sahu, D. Panda, S.K. Badjena, S.K. Sahoo, and P.K. Kar, Multicomponent Flux for Improved Penetration and Metallurgical Properties Using A-GTAW, *J. Mater. Eng. Perform.*, 2023, **32**(9), p 4237–4248
 13. R.S. Vidyarthi and D.K. Dwivedi, Microstructural and Mechanical Properties Assessment of the P91 A-TIG Weld Joints, *J. Manuf. Process.*, 2018, **31**, p 523–535. <https://doi.org/10.1016/j.jmapro.2017.12.012>
 14. S.W. Shyu, H.Y. Huang, K.H. Tseng, and C.P. Chou, Study of the Performance of Stainless Steel A-TIG Welds, *J. Mater. Eng. Perform.*, 2008, **17**, p 193–201
 15. H.Y. Huang, S.W. Shyu, K.H. Tseng, and C.P. Chou, Evaluation of TIG Flux Welding on the Characteristics of Stainless Steel, *Sci. Technol. Weld. Join.*, 2005, **10**(5), p 566–573
 16. K.D. Ramkumar, P.S. Goutham, V.S. Radhakrishna, A. Tiwari, and S. Anirudh, Studies on the Structure–Property Relationships and Corrosion Behaviour of the Activated Flux TIG Welding of UNS S32750, *J. Manuf. Process.*, 2016, **1**(23), p 231–241. <https://doi.org/10.1016/j.jmapro.2016.05.006>
 17. M. Ragavendran, M. Vasudevan, and N. Hussain, Study of the Microstructure, Mechanical Properties, Residual Stresses, and Distortion in Type 316LN Stainless Steel Medium Thickness Plate Weld Joints, *J. Mater. Eng. Perform.*, 2022, **31**(6), p 5013–5025
 18. K.C. Mills, B.J. Keene, R.F. Brooks, and A. Shirali, Marangoni Effects in Welding, *Philos. Trans. R. Soc. A Math. Phys. Eng. Sci.*, 1998, **356**(1739), p 911–925
 19. R.S. Vidyarthi, D.K. Dwivedi, and V. Muthukumar, Optimization of A-TIG Process Parameters Using Response Surface Methodology, *Mater. Manuf. Process.*, 2018, **33**(7), p 709–717. <https://doi.org/10.1080/10426914.2017.1303154>
 20. R.S. Vidyarthi and D.K. Dwivedi, Activating Flux Tungsten Inert Gas Welding for Enhanced Weld Penetration, *J. Manuf. Process.*, 2016, **22**, p 211–228. <https://doi.org/10.1016/j.jmapro.2016.03.012>
 21. C.L. Jenney and A. O'Brien, Welding Handbook—Welding Science and Technology, in *American Welding Society*, Cynthia L. Jenney, Ed., 9th ed., (Miami, FL 33126), American Welding Society, 1991, p 697–721
 22. T. Guo, Z. Dong, X. Nan, X. Liu, and L. Zhang, Effect of Welding Material on Microstructure and Properties of Welded Joints of Bridge Weathering Steel Q345qDNH, *Materwiss. Werksttech.*, 2022, **53**(11), p 1334–1346. <https://doi.org/10.1002/mawe.202200070>
 23. J. Zhang, W. Xin, G. Luo, R. Wang, and Q. Meng, Significant Influence of Welding Heat Input on the Microstructural Characteristics and Mechanical Properties of the Simulated CGHAZ in High Nitrogen V-Alloyed Steel, *High Temp. Mater. Process.*, 2020, **39**(1), p 33–44
 24. Q. Sun, H.-S. Di, J.-C. Li, B.-Q. Wu, and R.D.K. Misra, A Comparative Study of the Microstructure and Properties of 800 MPa Microalloyed C-Mn Steel Welded Joints by Laser and Gas Metal Arc Welding, *Mater. Sci. Eng. A*, 2016, **669**, p 150–158. <https://doi.org/10.1016/j.msea.2016.05.079>
 25. D.K. Adak, M. Mukherjee, and T.K. Pal, Development of a Direct Correlation of Bead Geometry, Grain Size and HAZ Width with the GMAW Process Parameters on Bead-on-Plate Welds of Mild Steel, *Trans. Indian Inst. Metals*, 2015, **68**, p 839–849
 26. D. Zhao, Y. Bezgans, N. Vdonin, L. Radionova, L. Glebov, and V. Bykov, Metallurgical and Mechanical Attributes of Gas Metal Arc Welded High-Strength Low-Alloy Steel, *Int. J. Adv. Manuf. Technol.*, 2023, **125**(3–4), p 1305–1323. <https://doi.org/10.1007/s00170-023-10807-5>
 27. M. Mirzaei, A. Khodabandeh, and H. Najafi, Effect of Active Gas on Weld Shape and Microstructure of Highly Efficient TIG Welded A516 Low Carbon Steel, *Trans. Indian Inst. Met.*, 2016, **69**(9), p 1723–1731
 28. R.S. Vidyarthi, D.K. Dwivedi, and M. Vasudevan, Influence of M-TIG and A-TIG Welding Process on Microstructure and Mechanical Behavior of 409 Ferritic Stainless Steel, *J. Mater. Eng. Perform.*, 2017, **26**(3), p 1391–1403
 29. P.K. Chaurasia, C. Pandey, A. Giri, N. Saini, and M.M. Mahapatra, A Comparative Study of Residual Stress and Mechanical Properties for FSW and TIG Weld on Structural Steel, *Arch. Metall. Mater.*, 2018, **63**, p 1019–1029. <https://doi.org/10.24425/122437>
 30. M.-S. Baek, K.-S. Kim, T.-W. Park, J. Ham, and K.-A. Lee, Quantitative Phase Analysis of Martensite-Bainite Steel Using EBSD and Its Microstructure, Tensile and High-Cycle Fatigue Behaviors, *Mater. Sci. Eng. A*, 2020, **785**, p 1–13. <https://doi.org/10.1016/j.msea.2020.139375>
 31. S. Zafar and A.K. Sharma, Structure-Property Correlations in Nanostructured WC-12Co Microwave Clad, *Appl. Surf. Sci.*, 2016, **370**, p 92–101. <https://doi.org/10.1016/j.apsusc.2016.02.114>
 32. E.V. Bobrynina, T.V. Larionova, T.S. Koltsova, S.A. Ginzburg, and V.G. Michailov, Effect of Alumina Addition on Weld Deposits Microstructure at the Welding of Carbon Steel, *Mater. Phys. Mech.*, 2018, **38**(1), p 26–32
 33. X.L. Wan, H.H. Wang, L. Cheng, and K.M. Wu, The Formation Mechanisms of Interlocked Microstructures in Low-Carbon High-Strength Steel Weld Metals, *Mater. Charact.*, 2012, **1**(67), p 41–51
 34. B.K. Khamari, S.S. Dash, S.K. Karak, and B.B. Biswal, Effect of Welding Parameters on Mechanical and Microstructural Properties of GMAW and SMAW Mild Steel Joints, *Ironmak. Steelmak.*, 2020, **47**(8), p 844–851
 35. T. Peng, C. Fu, Z. Qin, B. He, X. Hu, T. Zhu, B. Jiang, and Y. Liu, Microstructural Characterization and Mechanical Properties of a Q550W Weathering Steel Welded Joint under Different Heat Inputs, *J. Mater. Sci.*, 2022, **57**(34), p 16528–16540. <https://doi.org/10.1007/s10853-022-07688-6>

Publisher's Note Springer Nature remains neutral with regard to jurisdictional claims in published maps and institutional affiliations.

Springer Nature or its licensor (e.g. a society or other partner) holds exclusive rights to this article under a publishing agreement with the author(s) or other rightsholder(s); author self-archiving of the accepted manuscript version of this article is solely governed by the terms of such publishing agreement and applicable law.